Domain wall induced spin-polarized flat bands in antiferromagnetic topological insulators

E. K. Petrov,[1,2,*] V. N. Men'shov,[3,1,2] I. P. Rusinov,[1,2] M. Hoffmann,[4] A. Ernst,[4,5] M. M. Otrokov,[6,7] V. K. Dugaev,[8] T. V. Menshchikova,[1] and E. V. Chulkov[9,10,2,†]

[1]*Tomsk State University, 634050 Tomsk, Russia*
[2]*St. Petersburg State University, 199034 St. Petersburg, Russia*
[3]*NRC Kurchatov Institute, 123182 Moscow, Russia*
[4]*Institute for Theoretical Physics, Johannes Kepler University, 4040 Linz, Austria*
[5]*Max Planck Institute of Microstructure Physics, 06120 Halle, Germany*
[6]*Centro de Física de Materiales (CFM-MPC), Centro Mixto CSIC-UPV/EHU, 20018 Donostia-San Sebastián, Basque Country, Spain*
[7]*IKERBASQUE, Basque Foundation for Science, 48011 Bilbao, Spain*
[8]*Department of Physics and Medical Engineering, Rzeszów University of Technology, 35-959 Rzeszów, Poland*
[9]*Departamento de Polímeros y Materiales Avanzados: Física, Química y Tecnología, Facultad de Ciencias Químicas, Universidad del País Vasco UPV/EHU, 20080 San Sebastián/Donostia, Basque Country, Spain*
[10]*Donostia International Physics Center (DIPC), 20018 San Sebastián/Donostia, Spain*

(Received 6 January 2021; accepted 3 June 2021; published 21 June 2021)

A flat band in fermionic system is a dispersionless single-particle state with a diverging effective mass and nearly zero group velocity. These flat bands are expected to support exotic properties in the ground state, which might be important for a wide range of promising physical phenomena. For many applications, it is highly desirable to have such states in Dirac materials, but so far they have been reported only in some nonmagnetic Dirac systems. In this paper, we propose a realization of topologically protected spin-polarized flat bands generated by domain walls in planar magnetic topological insulators. Using first-principles material design, we suggest a family of intrinsic antiferromagnetic topological insulators with an in-plane sublattice magnetization and high Néel temperature. Such systems can host domain walls in a natural manner. For these materials, we demonstrate the existence of spin-polarized flat bands in the vicinity of the Fermi level and discuss their properties and potential applications.

DOI: 10.1103/PhysRevB.103.235142

I. INTRODUCTION

Modern technology proposals require considering quantum effects, which significantly expand functionality of new spintronic devices. Of great importance is realization of such physical phenomena as various Hall effects [1–3], a gate-tunable topological valley transport [4–8], and superconductivity [9–13]. In many cases, it can be attained by using specific electron states—flat bands [14]—which can arise either because of strong electronic correlations [15–18] or due to specific structural deformations [19–21]. In the absence of strongly correlated electrons, flat bands induced by strain were previously found in a number of nonmagnetic materials such as IV–VI semiconductor multilayers including topological crystalline insulators [22] and, recently, in twisted bilayer graphene [12,13,19,23–26]. In magnetic topological insulators (TIs), flat bands have not been reported so far.

Here we propose a way to generate flat bands in magnetic TI surfaces, where massless Dirac states and exchange fields can serve as a platform for creation of spin-polarized dispersionless states. The latter can appear due to magnetic domain walls (DWs) at the surface. However, most magnetic TIs are not well appropriated for such realization of flat bands, either because of a relatively low critical temperature (Curie or Néel temperature) or because of strong disorder effects in magnetically doped TIs. In this context, a universal platform can be provided by van der Waals (vdW)-layered antiferromagnetic topological insulators (AFM TIs) [27–35], where topological phase is governed by the $S = \Theta T_{1/2}$ symmetry (with Θ and $T_{1/2}$ being time-reversal and primitive-lattice translation operators, respectively), which allows $\mathbb{Z}_2$ topological classification [36].

As any other magnet, magnetic vdW compounds may manifest a domain structure [37] which ensures the existence of antiphase DWs. When a DW appears in AFM TI bulk, it can be terminated at the sample surface, significantly modifying surface band structure. For example, it was theoretically shown that DWs on the (0001) $MnBi_2Te_4$ surface host conducting states, which in the case of multiple domains may close the surface band gap [38]. Moreover, recently, Sass *et al.* reported on visualization and manipulation of DWs in out-of-plane AFM TI $MnBi_{2-x}Sb_xTe_4$ [39]. Magnetic DWs on AFM TI and FM TI surfaces could also be induced intentionally by a magnetic force microscope tip [40] or by spatially modulated external magnetic field due to Meissner repulsion from a bulk superconductor [41], as has been realized in Cr-doped

*evg.konst.petrov@gmail.com
†evguenivladimirovich.tchoulkov@ehu.eus

TI $(Bi,Sb)_2Te_3$. It was also demonstrated that DW magnetic texture on the surface of $MnBi_2Te_4$ with uniaxial anisotropy may be controlled by external magnetic field [42]. Additionally, Varnava *et al.* proposed a way to control quantum point junction on AFM TI surfaces [43]. Also note that a structural step can cause formation of antiphase DWs at rough surfaces of vdW AFM materials in which the sublattice magnetization direction alternates along the stacking direction.

In the present paper, using density functional theory (DFT) approach, which was successfully proven in first-principles design of various TIs [32,44–46], we suggest a number of AFM TI candidates with in-plane sublattice magnetization (planar AFM TIs in the following text) in the family of vdW systems MPn_2Ch_4 (M=Mn, V; Pn=Bi, Sb; Ch=Se, Te). Remarkably, the proposed V-based compounds have a significantly higher Néel temperature (in the range of 77–94 K) than Mn-based AFM TIs and related systems [45–49]. Employing tight-binding and model Hamiltonian approaches, we demonstrate that an antiphase DW induces a bound surface state with peculiar characteristics: it is topologically protected, dispersionless (flat), and exhibits out-of-plane spin polarization. Also, we show that by applying external magnetic field perpendicular to the surface, it is possible to tune the characteristics of this DW-induced state. In view of the unique combination of the two distinctive properties, flat bands, and planar magnetic TIs, we suggest several potential applications such as optical spin manipulations, anomalous Hall effect, and superconductive coupling between neighboring DWs.

II. RESULTS AND DISCUSSION

First, we determined the crystal structure and evaluated stability of all considered compounds (VBi_2Se_4, $VBi_2Te_2Se_2$, VBi_2Te_4, $VSb_2Te_2Se_2$, VSb_2Te_4, and $MnBi_2Te_2Se_2$). Since the related compounds tend to crystallize either in monoclinic ($C2/m$ space group) or rhombohedral [$R\bar{3}m$ space group, Fig. 1(a)] structure [50], we compared total energies of these two phases for each compound and found that the latter phase is energetically preferable (see Supplemental Material Table 2 [51]). The rhombohedral crystal structure can be represented by a sequence of hexagonal septuple layer (SL) blocks (e.g., Te–Bi–Se–V–Se–Bi–Te in the case of $VBi_2Te_2Se_2$), separated by vdW gaps. Stability of the compounds was considered as a complex characteristic concerned with two aspects: static (chemical, expressed in terms of bonding and energy) and dynamic. Static stability was evaluated in terms of total energy change after MCh bilayer (e.g., VSe) insertion into TI QL (e.g., Bi_2Se_3). The total energy drop suggests that such insertion and respective chemical bonding is energetically preferable. The dynamic aspect was considered in terms of phonon properties. We have calculated phonon spectra of isolated SL and bulk crystals for all compounds. It is clear that all the considered compounds are dynamically stable at zero temperature since there are no imaginary phonon frequencies (see Supplemental Material Fig. 2 [51]). Note the resulting VBi_2Te_4 crystal structure and phonon spectrum are in qualitative agreement with recent findings of Li *et al.* [56]. For details see Supplemental Material Note 1 and the respected Refs. [27,32,50–55].

Since interlayer magnetic coupling in similar vdW systems was found to be rather weak compared to the intralayer one [37,45,46], first we consider magnetic order in a single SL. Total energy calculations show ferromagnetic configuration to be preferable of the three considered magnetic configurations, ferromagnetic (FM), collinear antiferromagnetic (cAFM), and noncollinear antiferromagnetic (ncAFM). Taking into account interlayer magnetic coupling, total energy calculations reveal the antiparallel alignment of magnetic moments in adjacent SLs in the bulk materials (see Table I). These results are supported by the calculated exchange coupling parameters [Fig. 1(b)], which are mostly positive for the intralayer interaction [$J_{\parallel}^{0,i}$, Fig. 1(c)], indicating FM order, whereas the interlayer exchange parameters $J_{\perp}^{0,i}$ [Fig. 1(c)] are mostly negative, which is a distinct feature of interlayer AFM order. It also can be seen from integral exchange coupling parameters $J_{||}$ and $J_{\perp}$ (Table I).

To calculate the magnetocrystalline anisotropy energy (MAE), we examine three different spin quantization axis orientations: [0001] (out of plane), $[10\bar{1}0]$, and $[1\bar{1}00]$ (in plane). All considered compounds were found to tend to in-plane magnetization (see Table I). $MnBi_2Te_2Se_2$ is the only compound which stands out because its in-plane magnetization is due to the strong dipole-dipole contribution to MAE. We did not find any significant in-plane MAE.

We note the remarkable difference between the V- and Mn-containing compounds. The vdW systems under consideration possess a layered structure, where FM layers are well separated, and the interlayer exchange coupling $J_{\perp}$ is much weaker than the intralayer one $J_{\parallel}$. Typically, in layered systems, magnetocrystalline anisotropy and interlayer exchange coupling are essential for establishing a magnetic order at finite temperature. If a two-dimensional magnet has continuous symmetry in spin space, there is no spontaneous magnetization at finite temperatures [57,58]. For the proposed planar AFM TIs, within the framework of our calculation accuracy, we have not been able to identify the preferable orientation of Mn (or V) sublattice magnetization relative to crystallographic axes in the basal plane. It means that these planar AFM TIs are highly sensitive to orientational thermal fluctuations, which are expected to hinder the establishment of an intrinsic long-range magnetic order. This is in contrast to AFM TI $MnBi_2Te_4$, which is an Ising magnet with out-of-plane easy axis.

Our calculations show that the interlayer exchange coupling parameters in the V-containing compounds are several times larger than those in in $MnBi_2Te_2Se_2$ and $MnBi_2Te_4$ [45] [see Fig. 1(b) and Table I]. As follows from the density of states (DOS) plots, Mn $3d$ states are located far away from the Fermi level at $\simeq -6\,\mathrm{eV}$ and overlap only marginally with p bands of Bi, Te and/or Se, implying the main effect of Mn is to introduce the exchange field into SL block [see Fig. 1(e)]. In contrast, $3d$ states of vanadium hybridize significantly the p states of Bi/Te/Se within a wide energy range, which provides a very strong superexchange coupling between neighboring SLs across the vdW gap. As a result, vanadium compounds exhibit Nèel temperature T_N above 75 K, which is nearly four times higher than in the case of $MnBi_2Te_2Se_2$ (see Table I). It should be noted that

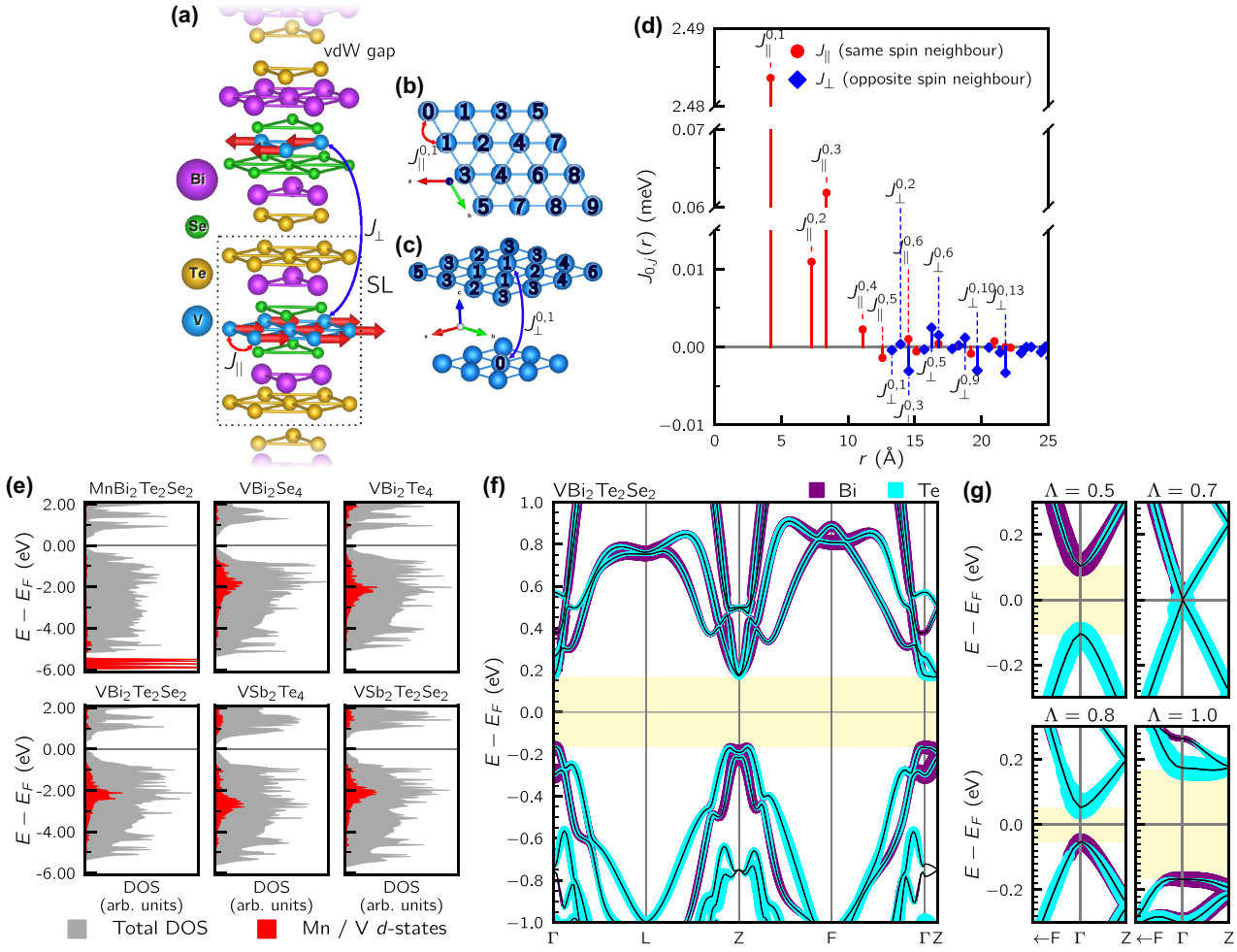

FIG. 1. (a) Crystal structure of bulk $VBi_2Te_2Se_2$. (b), (c) Schematic diagram of intralayer (b) and interlayer (c) exchange interactions. Blue balls represent V or Mn atoms. The numbers are the corresponding coordination sphere numbers. (d) Calculated exchange parameters $J^{0,j}$ for the intralayer [$J_{||}$, red circles, as depicted in (c)] and interlayer [$J_{\perp}$, blue diamonds, as depicted in (d)] pair interactions as a function of the V–V distance $r_{0,j}$ for $VBi_2Te_2Se_2$. (e) Bulk DOS of considered compounds (total and projected on Mn or V sites). Note, here the Fermi level is positioned at valence band top. (f) $VBi_2Te_2Se_2$ bulk band structure. The energies are given with respect to the Fermi level E_F. The band gap is highlighted with light yellow. The orbital composition is represented by colored lines, whose thickness is proportional to a specific site contribution to the electron state. (g) Bulk $VBi_2Te_2Se_2$ band structure in the vicinity of Γ point at different values of the SOC constant Λ (SOC is not taken into account with $\Lambda = 0$, and fully taken into account with $\Lambda = 1$). The orbital composition is also present.

predicted $MnBi_2Te_2Se_2$ T_N is slightly lower than in the case of out-of-plane magnetized AFM TI $MnBi_2Te_4$ (24.3 K) [45]. The Néel temperature can be roughly estimated within the standard spin-wave theory, $T_N^{\mathrm{SW}} \sim \frac{J_{\parallel} S^2}{\ln(\vartheta \frac{J_{\parallel}}{J_{\perp}})}$ (ϑ is a model parameter of the order of π^2). Then it is clear that such increase of the interlayer exchange coupling leads to three- or four-fold growth of the Néel temperature, which is in qualitative agreement with the calculation results presented in Table I. Thus, the enhanced interlayer interaction due to hybridization of the p states of Bi/Te/Se and the $3d$ states of V is crucial to stabilize long-range AFM order at such high temperatures.

Resulting magnetic structures were found to be stable against relatively small lattice parameter variations, which may be induced during growth process. We studied the dependence of both intra- and interlayer magnetic order and MAE on lattice constant values, which were varied within ±3 % from the equilibrium value, and U_{eff} values, which were varied ±1 eV from the adopted value (see Supplemental Material Table 4 [51]). Resulting equilibrium magnetic structures were found to be insensitive to such variations.

All considered compounds have typical narrow-gap semiconductor band structures with a band gap ranging from 11 meV up to 334 meV (see Fig. 1(f) and Table I, also see Supplemental Material Note 2 and Supplemental Material Fig. 2 [51]). We found that $MnBi_2Te_2Se_2$, $VBi_2Te_2Se_2$, VBi_2Te_4 and VSb_2Te_4, band gaps are inverted, which is confirmed by $\mathbb{Z}_2$ invariant calculations, which show $\mathbb{Z}_2 = 1$. In contrast, VBi_2Se_4 and $VSb_2Te_2Se_2$ were found to have a trivial insulating bulk band structure with $\mathbb{Z}_2 = 0$. To track the band gap inversion genesis, we calculated $VBi_2Te_2Se_2$ bulk band structures at different spin-orbit coupling (SOC) with the Λ parameter ranging from 0 (SOC not accounted) to 1 (SOC fully accounted). The results clearly show that the orbital composition of the band gap edges at $\Lambda < 0.7$ is not

TABLE I. Rows 1 and 2: Differences in total energies between FM ($E^{\text{intra}}_{\text{FM}}$), cAFM ($E^{\text{intra}}_{\text{cAFM}}$), and ncAFM ($E^{\text{intra}}_{\text{ncAFM}}$) 1-SL slab magnetic configurations. In FM and cAFM cases, spins are oriented out of plane, while in ncAFM case spins are in (0001) plane in the way so each pair of neighbouring spins form a 120° angle. Row 3: Differences in total energies between FM ($E^{\text{inter}}_{\text{FM}}$) and AFM ($E^{\text{inter}}_{\text{AFM}}$) bulk magnetic orders. Rows 4 and 5: Integral exchange coupling parameters $J_{||}$ (intralayer) and $J_{\perp}$ (interlayer). Row 6: Differences in total energies of in-plane ($E_{||}$) and out-of-plane ($E_{\perp}$) spin orientations. Row 7: Same as row 5, but including the dipole-dipole contribution (E_{dip}). Rows 8–11: Magnetic moments on Mn or V sites, calculated bulk Néel temperatures T_N, bulk band gap, and $\mathbb{Z}_2$ invariant value, respectively.

	Compound	$MnBi_2Te_2Se_2$	VBi_2Se_4	$VBi_2Te_2Se_2$	VBi_2Te_4	$VSb_2Te_2Se_2$	VSb_2Te_4,	$MnBi_2Te_4$ [45]
1	$E^{\text{intra}}_{\text{cAFM}} - E^{\text{intra}}_{\text{FM}}$ (meV/f.u.)	+5.1	+9.2	+13.9	+16.6	+11.6	+12.3	+5.7
2	$E^{\text{intra}}_{\text{ncAFM}} - E^{\text{intra}}_{\text{FM}}$ (meV/f.u.)	+6.8	+17.6	+25.7	+29.9	+14.9	+15.5	+7.4
3	$E^{\text{inter}}_{\text{AFM}} - E^{\text{inter}}_{\text{FM}}$ (meV/f.u.)	−0.770	−0.164	−0.320	−0.677	−0.387	−0.788	−1.40
4	$J_{||}$, meV *	3.52	16.12	14.14	20.50	18.29	22.03	–
5	$J_{\perp}$, meV *	−0.08	−0.27	−0.16	−0.45	−0.54	−0.9	–
6	$E_{||} - E_{\perp}$ (meV/f.u.)	+0.053	−0.092	−0.022	−0.176	−0.004	−0.087	+0.171
7	$E_{||} - E_{\perp} + E^{\text{dip}}_{||}$ (meV/f.u.)	−0.078	−0.148	−0.074	−0.224	−0.059	−0.138	+0.128
8	Magnetic moment (μ_B)	4.622	2.924	2.933	2.956	2.936	2.966	4.607
9	T_N (K)	18.6	80.88	77.1	78.6	91.6	93.9	25.4/24.3 **
10	Band gap (meV)	256	55	334	233	11	125	220
11	$\mathbb{Z}_2$	1	0	1	1	0	1	1

*Note that the quantities in rows 1–3 and the exchange coupling parameters in rows 4 and 5 are calculated with two very different methods and codes. See Methods section for details.
**Calculated/experimental values.

inverted yet: The highest valence band is primarily formed by Te states, and the lowest conduction band by Bi states. At $\Lambda \approx 0.7$ the band gap vanishes and at $\Lambda > 0.7$ it reopens with inverted edges [see Fig. 1(g)]. The inversion is caused mainly by p_z states of ions close to vdW gaps (Te and Bi), similar to tetradymite-like non-magnetic TIs. The other topologically nontrivial compounds under study exhibit similar behavior. Note, the resulting VBi_2Te_4 magnetic and bulk band structures are in qualitative agreement with previously reported data [56].

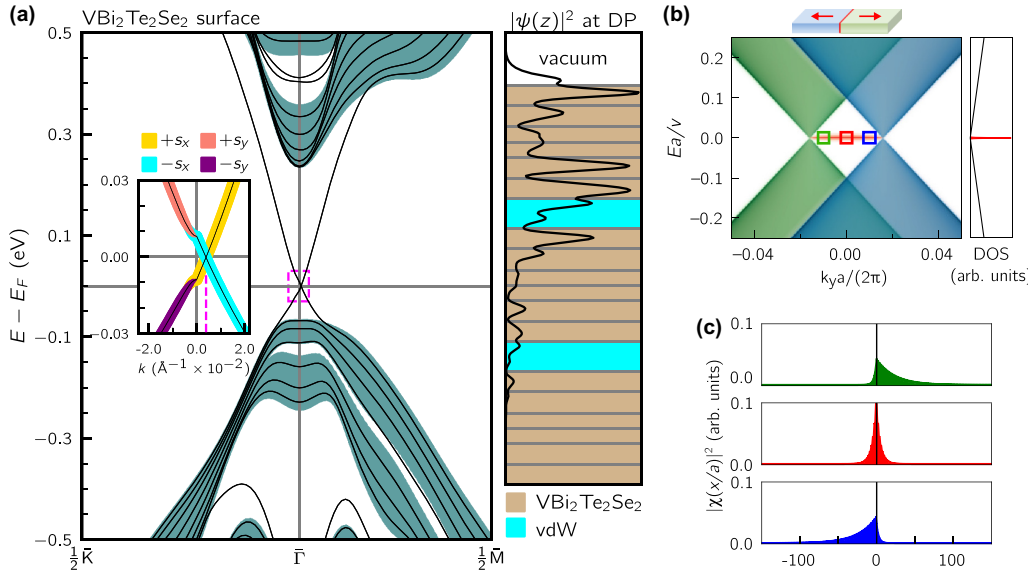

FIG. 2. (a) $VBi_2Te_2Se_2$ (0001) surface band structure near the Fermi level. Sea-blue areas correspond to bulk bands, projected on two-dimensional Brillouin zone (2D BZ), and the black lines to surface bands. Surface spin texture (inset on the left) is represented by color lines, which thickness is proportional to spin projection value. The right panel depicts $|\psi(z)|^2$ at Dirac point (DP), with ψ being one-electron wave function. (b) Spectral density of the electron states on the surface containing single antiphase DW. For generality, the scales of the axes are presented in dimensionless units constructed by combination of energy and momentum with model parameters. The spectral density corresponding to the left (right) semi-infinite region is represented by blue (green) color, projected on 1D BZ, and the flat band by red color. DOS at the $\bar{\Gamma}$ point of 2D BZ is shown on the right side of the panel. Black solid line represents DOS for the Dirac cones, the red peak is DOS for the flat band. The magnetic configuration is schematically illustrated on the top, where red arrows in blue and green regions indicate magnetization directions in the vicinity of DW. (c) The charge density distribution of zero-energy bound states as a function of distance from the DW. The energy-momenta values are marked by color squares in (b).

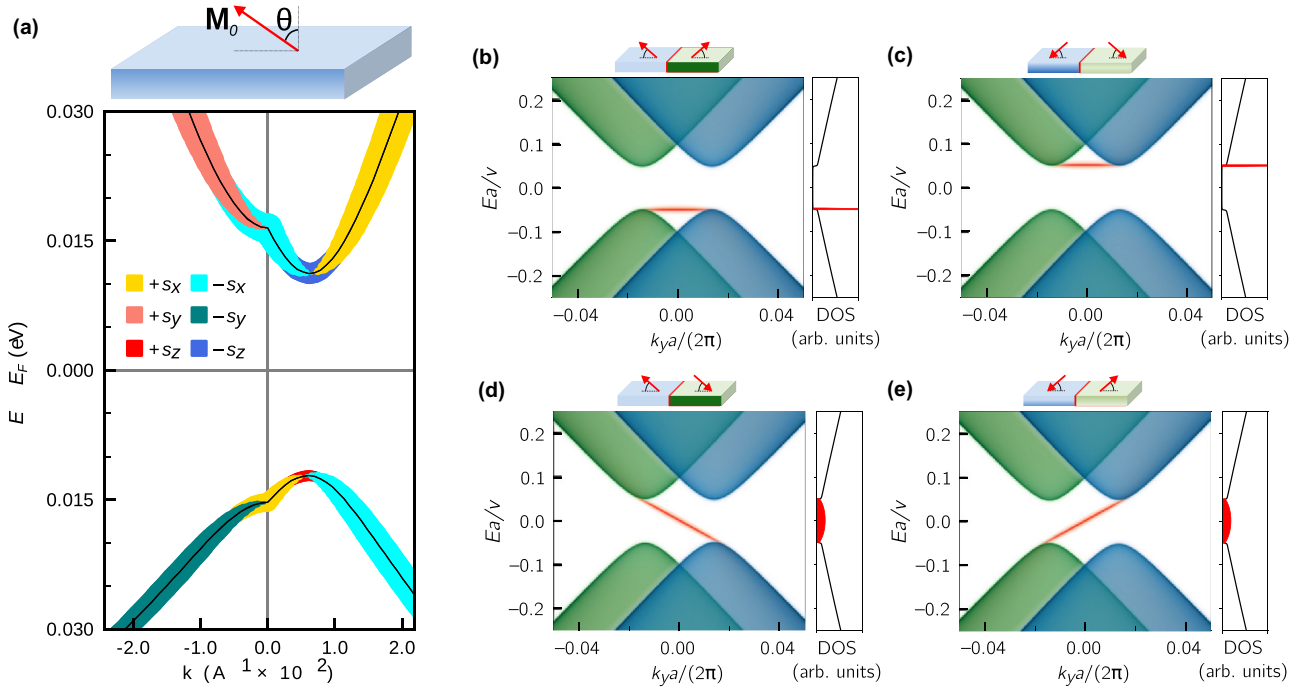

FIG. 3. (a) $MnBi_2Te_2Se_2$ (0001) surface band structure near the Fermi level in the case of mixed magnetization. (b)–(e) The same as Fig. 2(b) but with additional negative (b), positive (c), and opposite (d), (e) out-of-plane magnetization components.

The inversion ensures the appearance of a topological surface state on the (0001) surface of $MnBi_2Te_2Se_2$, $VBi_2Te_2Se_2$, VBi_2Te_4 and VSb_2Te_4. As an example, Fig. 2(a) presents the spectrum of such surface state of $VBi_2Te_2Se_2$. As may be seen from the inset, the Dirac point is slightly shifted from the $\bar{\Gamma}$. Since the topological surface state is mainly localized within the topmost SL, the direction of the shift is normal to the magnetization **M** of that SL, and its value is proportional to its magnitude $|\mathbf{M}|$. Such behavior of the topological surface state under in-plane magnetization is consistent with that reported in magnetically doped TIs [59], TI-based magnetic heterostructures [32], AFM TIs (i.e., $MnBi_2Te_4$) [60], and TIs under external magnetic field [61]. Since the surfaces were modeled within the repeating slabs model (see Methods), slab thickness directly affects the resulting band structure. Slabs of an even (odd) number of SLs produce surfaces (top and bottom) with antiparallel (parallel) magnetizations, which leads to parallel (antiparallel) Dirac points shift since the Dirac cones have opposite chiralities. The displayed surface band structures were modeled with eight SL slabs, so both Dirac points are shifted in the same direction.

We must note here that the above described results are obtained on the assumption that the (0001) surface SL is accommodated by the bulk interlayer AFM ordering while preserving intralayer FM order. This is mostly due to a large distance between Mn or V atomic layers and a large vdW gap, which result in weak exchange coupling between adjacent SLs. If the crystal cleaves along a vdW gap, Mn, or V magnetic moments are not very sensitive to the lack of coordination number in the surface vicinity and magnetic order does not differ from the one in bulk. Surface band structures of the other topologically nontrivial compounds can be found in Supplemental Material Note 2 and Supplemental Material Figure 3 [51]. Thus, our DFT calculations demonstrate that all the topologically nontrivial compounds under study are characterized by a gapless Dirac state with helical spin texture on the ideal (0001) surface.

The right panel in Fig. 2(a) indicates that the Dirac fermions are predominantly localized within the topmost SL. Their behavior, affected by the exchange field, $\sim\mathbf{M}$, originated from the local moments of the same SL, can be described by the effective two-dimensional Hamiltonian

$$H(\mathbf{k}) = \upsilon(k_y\sigma_x - k_x\sigma_y) - j(M_x\sigma_x + M_y\sigma_y) - j_\perp\sigma_z M_z, \quad (1)$$

where υ is the Fermi velocity, $\mathbf{k} = (k_x, k_y)$ is the in-plane momentum, σ_x, σ_y, and σ_z are the Pauli matrices acting in spin space. In the Hamiltonian Eq. (1), the warping term is neglected because its effect is negligible due to a relatively small Dirac point shift from the $\bar{\Gamma}$ point. Nevertheless, we have investigated the effect of warping term on the results (please see Supplemental Material Note 3 and the respected Refs. [51,62,63]). For the definiteness, we assign $j, j_\perp > 0$ and $\upsilon > 0$. The first term captures the presence of Dirac-like quasiparticles with linear spectrum and perfect spin-momentum locking. The effective exchange integrals j and $j_\perp$ couple the surface quasiparticle spins with the local magnetization of the topmost SL, $\mathbf{M} = (M_x, M_y, M_z)$, which can generically be in an arbitrary direction. In the case of the spatially homogeneous magnetization **M**, the energy spectrum of the Hamiltonian Eq. (1) is given by the relation $E^2(\mathbf{k}) = (\upsilon k_x + jM_y)^2 + (\upsilon k_y - jM_x)^2 + j_\perp^2 M_z^2$.

To explore how the spatially inhomogeneous magnetization $\mathbf{M}(x, y)$ affects the surface state of an AFM TI, we use the model of a single rigid DW. In the Hamiltonian Eq. (1), the (x, y) plane is assumed to be divided

in two semi-infinite uniformly ordered regions with opposite polarizations, thus $\mathbf{M}(x, y)$ changes its direction upon crossing the linear boundary $x = 0$, but keeps its magnitude. We specify the space profile of the DW in the form $\mathbf{M}(x, y) = M_0(\sin\theta\,\mathrm{sgn}(x), 0, \cos\theta)$, where $|\mathbf{M}(x, y)| = M_0 = \mathrm{const}$. Here the magnetization vector can rotate through an angle $\pi - \theta$ out of the plane. Due to the periodicity along the **y** direction, the momentum k_y is a good quantum number. To describe the fermion state hosted by the DW, we apply the analytical approach (see Supplemental Material Note 4 for details [51]) as well as the numerical tight-binding calculations.

In following, we address the planar AFM TI surface where the local moments lie in the plane and have opposite directions in the right and left domains, i.e., $\mathbf{M}(x, y) = M_0(\mathrm{sgn}(x), 0, 0)$ [see Fig. 2(b)]. The surface with such tail-to-tail DW harbors two types of quasiparticles manifesting utterly distinct behaviors: on the one hand, 2D *massless* Dirac fermions; on the other hand, 1D heavy fermions with *infinitely large effective mass*. The pair of Dirac cones, shifted to momenta $\pm k_0$, where $k_0 = \frac{jM_0}{\upsilon}$, with respect to the Brillouin zone center, corresponds to the two semi-infinite domains with opposite magnetization. The flat band exists within the interval between the Dirac nodes, $|k_y| < k_0$. Remarkably, this particular state does not disperse in k_y at zero energy, $E(\mathbf{k}) = 0$, forming a sharp peak in DOS at $E = 0$ against the linear dependence of Dirac fermions DOS [see right panel on Fig. 2(b)]. This flat-band state is topologically protected, which originates from the Berry phase of π for each Dirac node and, therefore, cannot be destroyed by DW imperfections (see the respective discussion in Supplemental Material Note 5 [51]). The probability density of the flat band decays exponentially away from the DW on the scale $|\chi(x)|^2 \sim \exp(-2k_0|x|)$ as demonstrated in Fig. 2(c). Furthermore, the dispersionless state is fully spin polarized. Therefore, the expectation value of the spin angular momentum is zero for the in-plane components, $\langle\sigma_x\rangle = \langle\sigma_y\rangle = 0$, but it is nonzero in the direction normal to the surface, i.e., normal to the easy plane, $\langle\sigma_z\rangle \neq 0$. Note the spin polarization of the flat band induced by head-to-head DW is antiparallel to the one induced by tail-to-tail DW.

In general, surface magnetization cannot be attached tightly to the plane. For example, Mn or V sublattice magnetization of a planar AFM TI can acquire nonzero out-of-plane component M_z due to external magnetic field or magnetic proximity effect. In the case of an AFM TI surface hosting an isolated DW with the spatial profile $\mathbf{M}(x, y) = M_0(\sin\theta\,\mathrm{sgn}(x), 0, \cos\theta)$, the uniform out-of-plane component M_z breaks the spin degeneracy opening the energy gaps at the Dirac points $\pm k_0 \sin\theta$ in the spectrum [see Figs. 3(b) and 3(c)]. As follows from the figures, tail-to-tail DW creates the dispersionless state with the energy $E = j_\perp M_z$ ($E = -j_\perp M_z$), which connects the band edges of the two gapped cones with dispersion $E^2(\mathbf{k}) = (\upsilon k_x)^2 + \upsilon^2(k_y \pm k_0 \sin\theta)^2 + j_\perp^2 M_z^2$. Indeed, we observe such gap opening within *ab initio* calculations [see Fig. 3(a)]. We modeled such out-of-plane Zeeman perturbation with simultaneous spin rotation in the perfect planar AFM phase. Correspondingly, the keen peak in the DOS appears just at the band edge. It should be noted that nonzero M_z shifts the energy and reduces the momentum interval of the flat band but does not change the spin polarization direction and flatness of the DW state.

According to the numerical simulations, $MnBi_2Te_2Se_2$ is a vdW AFM TI with in-plane anisotropy, whereas $MnBi_2Te_4$ has been identified as an out-of-plane AFM TI. Therefore, it is natural to assume that the solid solution $MnBi_2(Te_{1-x}Se_x)_4$ at the certain concentration value $0 < x < \frac{1}{2}$ would have AFM order with the sublattice magnetization directed to the angle $0 < |\theta| < \frac{\pi}{2}$ to the basal plane, keeping nontrivial invariant $\mathbb{Z}_2 \neq 0$. In our approach, in the presence of an antiphase DW, the surface magnetization of such a material is modeled with the spatial profile $\mathbf{M}(x, y) = M_0(\sin\theta\,\mathrm{sgn}(x), 0, \cos\theta\,\mathrm{sgn}(x))$. Interestingly, the DW-induced bound state is associated with the linear spectral branch, $E(k) = \pm\frac{j_\perp}{j}\cos\theta\,\upsilon k_y$, which spans the magnetic gap, $2|j_\perp M_0 \cos\theta|$, and connects edges of the bands originated from the opposite magnetic domains [see Figs. 3(d) and 3(e)].

Thus, in the absence of out-of-plane magnetic moment component M_z, the flat band connects two Dirac points [see Fig. 2(b)]. Under nonzero M_z or under external magnetic field, a gap opens at the Dirac points. Here two different scenarios are possible: (1) If the M_z sign is the same for both domains, the flat band survives but connects either valence or conduction bands [see Figs. 3(b) and 3(c)]. (2) If M_z signs are opposite for the two domains, then the flat band evolves to a chiral state connecting valence and conduction bands [see Fig. 3(d) and 3(e)]. In the case of a small M_z component, the Dirac point gap will be small too, and the chiral state will be nearly flat. This opens wide possibilities to control the properties of the DW-bound state by changing its effective mass from zero to infinity. We note, however, that the flat character of the DW-bound state is provided by chiral symmetry of the Hamiltonian. If one explicitly accounts atomic and magnetic structure of the DW, reasonable variation in energy can be expected and the flat band may not be completely flat. Also, we would like to note that properties of the flat-band state depend on temperature, namely, its span across 1D BZ, real space localization, and its width (see Supplemental Material Note 6 [51]).

III. CONCLUSION

In this paper, we proposed the tetradymitelike planar AFM TI family and by means of *ab initio* calculations we determined their equilibrium crystal, electronic, and magnetic structures. We found all considered compounds to be layered antiferromagnets with in-plane magnetization.

The proposed V-based compounds have Néel temperature in the range of 77–94 K, which is significantly higher than in the case of Mn-based AFM TIs. We showed that the critical temperature can strongly depend on the chemical composition, in particular, Sb–containing compounds show increasing Néel temperature of almost 20 K with respect to Bi ones. All the considered compounds possess a typical semiconductor bulk band structure. We found bulk $MnBi_2Te_2Se_2$, $VBi_2Te_2Se_2$, VBi_2Te_4 and VSb_2Te_4, to exhibit $\mathbb{Z}_2 = 1$ and an AFM TI phase. Such compounds are characterized by a gapless surface state on the (0001) surface, which has helical spin texture similar to nonmagnetic TIs. The topmost SL magnetization shifts Dirac point from $\bar{\Gamma}$.

We demonstrated that magnetic inhomogeneities like DWs on the (0001) surface can prompt the appearance of topological one-dimensional flat bands, which give rise to a

sharp peak in the DOS near the Fermi level. We showed that these flat band states can be effectively tuned by applying external magnetic field perpendicular to the surface plane. In this context, AFM TIs with in-plane sublattice magnetization provide a very special and rich platform to study surface electronic properties.

The appearance of flat bands with fully spin-polarized electron states leads to some unusual effects in these materials. For example, optical excitation of electrons from the flat band can lead to an observable spin-resolved photoelectric effect, e.g., spin- and valley-polarized currents.

The flat-band state can manifest itself in the anomalous Hall effect on a single DW. Indeed, free electrons in the topmost SL, transmitted through the DW, are subjected to out-of-plane polarization associated with the state. Due to SOC, it can lead to the transverse current.

Since the Fermi energy is pinned to the flat-band energy, we can also predict the appearance of superconductivity related to the coupling of heavy electrons from neighboring DWs. Indeed, the electrons from neighboring DWs have opposite spin directions, and the interaction between them via phonons can be rather strong since the electron localization allows us to release the momentum conservation condition in electron-phonon interactions. It should also be noted that intra-DW electron-electron repulsion does not affect the superconductivity related to pairing at different DWs [64]. Finally, we can expect an enhancement of the critical temperature for superconductivity transition thanks to the infinite electron DOS.

ACKNOWLEDGMENTS

E.K.P. acknowledges support from RFBR within Research Projects No. 18-32-00728 (the study of V-based compounds crystal, magnetic, and band structures) and No. 19-32-90250 (the study of V-based compound critical temperatures). V.N.M. acknowledges support from Russian Science Foundation within Research Project No. 18-12-00169-p (the study of DWs by the model Hamiltonian approach). T.V.M. and I.P.R. acknowledge support from the Ministry of Education and Science of the Russian Federation within State Task No. 0721-2020-0033 (the study of DWs by tight-binding approaches). A.E. acknowledges support from DFG through Priority Program No. SPP1666 (Topological Insulators) and OeAD Grants No. HR 07/2018 and No. PL 03/2018. V.K.D. acknowledges support from the National Science Center of Poland under Project No. DEC-2017/27/B/ST3/02881. E.V.C. acknowledges support from Saint Petersburg State University (Project ID No. 73028629). Calculations performed at the Research Park of Saint-Petersburg State University Computing Center (http://www.cc.spbu.ru/) and SKIF-Cyberia supercomputer of National Research Tomsk State University.

First-principles calculations were performed by E.K.P. and A.E. Monte Carlo simulations were done by M.H. The model Hamiltonian approach was developed by V.N.M. Tight-binding calculations were performed by I.P.R. Figures were produced by E.K.P., T.V.M., and I.P.R. Project planning was done by E.V.C., E.K.P., T.V.M., I.P.R., V.N.M., and A.E. All authors contributed to the discussion and to writing the paper.

APPENDIX: METHODS

Bulk crystal structures, magnetic order, MAE, bulk and surface band structures were investigated using the projector augmented-wave method [65] implemented in the VASP package [66–68]. Exchange-correlation effects were taken into account using Perdew-Burke-Ernzerhof generalized gradient approximation (GGA) [69]. Spin-orbit coupling was treated using the second variation technique [70]. The DFT-D3 method [71] was used to accurately describe the vdW interaction. The plane-wave energy cutoff was chosen exclusively for each compound (280 eV for $MnBi_2Te_2Se_2$, 240 eV for VBi_2Se_4, $VBi_2Te_2Se_2$ and VBi_2Te_4, 275 eV for $VSb_2Te_2Se_2$, and 250 eV for VSb_2Te_4,) and was kept constant through all calculations. The energy convergence criterion was set to 10^{-6} eV for all types of calculations except magnetocrystalline anisotropy study, for which it was decreased down to 10^{-7} eV. FM phases were modeled using a rhombohedral cell containing one Mn or V atom (1 f.u.) and monoclinic cell containing 4 Mn or V atoms (4 f.u.), respectively. AFM bulk phases were modeled using a rhombohedral cell containing two Mn atoms (2 f.u.) and a hexagonal cell containing six Mn atoms (6 f.u.). Collinear AFM and non-collinear AFM phases were modeled using rectangular $(1 \times \sqrt{3})$ and $(\sqrt{3} \times \sqrt{3})R30^\circ$ cells, respectively. All ferromagnetic slabs were studied using convenient hexagonal cells. Magnetocrystalline anisotropy studies were performed on the same hexagonal cell. Surfaces were modeled within the repeating slabs model, i.e., surface band structures are derived from direct DFT calculations of 8-SL (56 atomic layers) thick slabs.

Mn and V $3d$ states were treated using a GGA + U approach [72,73]. The values of U_{eff} were calculated using a linear response technique proposed by Cococcioni and de Gironcoli [74]. Adopted U values were 5.3, 4.8, 5.0, 4.7, 4.6, and 5.0 eV for $MnBi_2Te_2Se_2$, VBi_2Se_4, $VBi_2Te_2Se_2$, VBi_2Te_4, $VSb_2Te_2Se_2$, and VSb_2Te_4, respectively.

Calculations of $\mathbb{Z}_2$ invariants were performed using Z2PACK [75–78]. Phonon spectra were calculated using the PHONOPY package [79].

To obtain exchange coupling parameters, we used the magnetic force theorem [80] as implemented within the multiple scattering theory package HUTSEPOT [81], along with the full charge density approximation [82]. They were confirmed by Monte Carlo simulations based on the classical Heisenberg Hamiltonian with the obtained exchange coupling parameters from above. The heat capacity was used as indication for the magnetic phase transition. Monte Carlo results were checked for convergence of all simulation parameters, i.e., simulation size and Monte Carlo steps. More technical details can be found in Ref. [81].

The introduced toy model, Eq. (1), may be directly implemented to analytically describe low-energy fermions at the surface of planar AFM TI for various inhomogeneous magnetization configurations in the uppermost SL. This consideration is restricted to simple configurations (in the form of rigid one-dimensional DWs), which allowed us to find the exact solution for the corresponding eigenstate problem. Indeed, we have obtained a modification of the energy spectrum and the envelope wave function

spatial profile of the surface states caused by a magnetic DW presence. These results are consistent with those of a tight-binding study of the model regularized on square lattice.

[1] C. L. Kane and E. J. Mele, Phys. Rev. Lett. **95**, 226801 (2005).
[2] C. L. Kane and E. J. Mele, Phys. Rev. Lett. **95**, 146802 (2005).
[3] H. Weng, R. Yu, X. Hu, X. Dai, and Z. Fang, Adv. Phys. **64**, 227 (2015).
[4] L. Ju, Z. Shi, N. Nair, Y. Lv, C. Jin, J. Velasco Jr, C. Ojeda-Aristizabal, H. A. Bechtel, M. C. Martin, A. Zettl *et al.*, Nature (London) **520**, 650 (2015).
[5] T. Y. Hung, K. Y. Camsari, S. Zhang, P. Upadhyaya, and Z. Chen, Sci. Adv. **5**, eaau6478 (2019).
[6] E. Mania, A. Cadore, T. Taniguchi, K. Watanabe, and L. Campos, Commun. Phys. **2**, 6 (2019).
[7] M. Sui, G. Chen, L. Ma, W.-Y. Shan, D. Tian, K. Watanabe, T. Taniguchi, X. Jin, W. Yao, D. Xiao *et al.*, Nat. Phys. **11**, 1027 (2015).
[8] X.-T. He, E.-T. Liang, J.-J. Yuan, H.-Y. Qiu, X.-D. Chen, F.-L. Zhao, and J.-W. Dong, Nat. Commun. **10**, 872 (2019).
[9] B. Lian, Z. Wang, and B. A. Bernevig, Phys. Rev. Lett. **122**, 257002 (2019).
[10] X. Lu, P. Stepanov, W. Yang, M. Xie, M. A. Aamir, I. Das, C. Urgell, K. Watanabe, T. Taniguchi, G. Zhang *et al.*, Nature (London) **574**, 653 (2019).
[11] H. C. Po, L. Zou, A. Vishwanath, and T. Senthil, Phys. Rev. X **8**, 031089 (2018).
[12] M. Yankowitz, S. Chen, H. Polshyn, Y. Zhang, K. Watanabe, T. Taniguchi, D. Graf, A. F. Young, and C. R. Dean, Science **363**, 1059 (2019).
[13] Y. Cao, V. Fatemi, S. Fang, K. Watanabe, T. Taniguchi, E. Kaxiras, and P. Jarillo-Herrero, Nature (London) **556**, 43 (2018).
[14] D. Leykam, A. Andreanov, and S. Flach, Adv. Phys.: X **3**, 1473052 (2018).
[15] E. H. Lieb, Phys. Rev. Lett. **62**, 1201 (1989).
[16] A. Mielke, J. Phys. A: Math. Gen. **24**, 3311 (1991).
[17] A. Tanaka and H. Ueda, Phys. Rev. Lett. **90**, 067204 (2003).
[18] H. Katsura, I. Maruyama, A. Tanaka, and H. Tasaki, Europhys. Lett. **91**, 57007 (2010).
[19] Y. Cao, V. Fatemi, A. Demir, S. Fang, S. L. Tomarken, J. Y. Luo, J. D. Sanchez-Yamagishi, K. Watanabe, T. Taniguchi, E. Kaxiras *et al.*, Nature (London) **556**, 80 (2018).
[20] N. Y. Fogel, E. I. Buchstab, Y. V. Bomze, O. Yuzephovich, M. Y. Mikhailov, A. Y. Sipatov, E. Pashitskii, R. I. Shekhter, and M. Jonson, Phys. Rev. B **73**, 161306(R) (2006).
[21] O. Mironov, B. Savitskii, A. Y. Sipatov, A. Fedorenko, A. Chirkin, S. Chistyakov, and L. Shpakovskaya, Zh. Eksp. Teor. FIz. **48**, 100 (1988) [JETP Lett. **48**, 106 (1988)].
[22] E. Tang and L. Fu, Nat. Phys. **10**, 964 (2014).
[23] K. Kim, A. DaSilva, S. Huang, B. Fallahazad, S. Larentis, T. Taniguchi, K. Watanabe, B. J. LeRoy, A. H. MacDonald, and E. Tutuc, Proc. Natl. Acad. Sci. U.S.A. **114**, 3364 (2017).
[24] A. L. Sharpe, E. J. Fox, A. W. Barnard, J. Finney, K. Watanabe, T. Taniguchi, M. Kastner, and D. Goldhaber-Gordon, Science **365**, 605 (2019).
[25] H. Yoo, R. Engelke, S. Carr, S. Fang, K. Zhang, P. Cazeaux, S. H. Sung, R. Hovden, A. W. Tsen, T. Taniguchi *et al.*, Nat. Mater. **18**, 448 (2019).
[26] T. M. R. Wolf, J. L. Lado, G. Blatter, and O. Zilberberg, Phys. Rev. Lett. **123**, 096802 (2019).
[27] J. A. Hagmann, X. Li, S. Chowdhury, S.-N. Dong, S. Rouvimov, S. J. Pookpanratana, K. M. Yu, T. A. Orlova, T. B. Bolin, C. U. Segre *et al.*, New J. Phys. **19**, 085002 (2017).
[28] C. Gong, L. Li, Z. Li, H. Ji, A. Stern, Y. Xia, T. Cao, W. Bao, C. Wang, Y. Wang *et al.*, Nature (London) **546**, 265 (2017).
[29] B. Huang, G. Clark, E. Navarro-Moratalla, D. R. Klein, R. Cheng, K. L. Seyler, D. Zhong, E. Schmidgall, M. A. McGuire, D. H. Cobden *et al.*, Nature (London) **546**, 270 (2017).
[30] M. Otrokov, T. Menshchikova, M. Vergniory, I. Rusinov, A. Y. Vyazovskaya, Y. M. Koroteev, G. Bihlmayer, A. Ernst, P. Echenique, A. Arnau *et al.*, 2D Mater. **4**, 025082 (2017).
[31] M. M. Otrokov, T. V. Menshchikova, I. P. Rusinov, M. G. Vergniory, V. M. Kuznetsov, and E. V. Chulkov, JETP Lett. **105**, 297 (2017).
[32] T. Hirahara, S. V. Eremeev, T. Shirasawa, Y. Okuyama, T. Kubo, R. Nakanishi, R. Akiyama, A. Takayama, T. Hajiri, S.-i. Ideta *et al.*, Nano Lett. **17**, 3493 (2017).
[33] D. R. Klein, D. MacNeill, J. L. Lado, D. Soriano, E. Navarro-Moratalla, K. Watanabe, T. Taniguchi, S. Manni, P. Canfield, J. Fernández-Rossier *et al.*, Science **360**, 1218 (2018).
[34] T. Song, X. Cai, M. W.-Y. Tu, X. Zhang, B. Huang, N. P. Wilson, K. L. Seyler, L. Zhu, T. Taniguchi, K. Watanabe *et al.*, Science **360**, 1214 (2018).
[35] Z. Wang, I. Gutiérrez-Lezama, N. Ubrig, M. Kroner, M. Gibertini, T. Taniguchi, K. Watanabe, A. Imamoğlu, E. Giannini, and A. F. Morpurgo, Nat. Commun. **9**, 2516 (2018).
[36] R. S. K. Mong, A. M. Essin, and J. E. Moore, Phys. Rev. B **81**, 245209 (2010).
[37] M. A. McGuire, H. Dixit, V. R. Cooper, and B. C. Sales, Chem. Mater. **27**, 612 (2015).
[38] K. F. Garrity, S. Chowdhury, and F. M. Tavazza, Phys. Rev. Mater. **5**, 024207 (2021).
[39] P. M. Sass, W. Ge, J. Yan, D. Obeysekera, J. Yang, and W. Wu, Nano Lett. **20**, 2609 (2020).
[40] K. Yasuda, M. Mogi, R. Yoshimi, A. Tsukazaki, K. Takahashi, M. Kawasaki, F. Kagawa, and Y. Tokura, Science **358**, 1311 (2017).
[41] I. T. Rosen, E. J. Fox, X. Kou, L. Pan, K. L. Wang, and D. Goldhaber-Gordon, npj Quantum Mater. **2**, 69 (2017).
[42] P. M. Sass, J. Kim, D. Vanderbilt, J. Yan, and W. Wu, Phys. Rev. Lett. **125**, 037201 (2020).
[43] N. Varnava, J. H. Wilson, J. Pixley, and D. Vanderbilt, arXiv:2008.03316.
[44] S. V. Eremeev, G. Landolt, T. V. Menshchikova, B. Slomski, Y. M. Koroteev, Z. S. Aliev, M. B. Babanly, J. Henk, A. Ernst, L. Patthey *et al.*, Nat. Commun. **3**, 635 (2012).
[45] M. Otrokov, I. Klimovskikh, H. Bentmann, D. Estyunin, A. Zeugner, Z. Aliev, S. Gaß, A. Wolter, A. Koroleva, A. Shikin *et al.*, Nature (London) **576**, 416 (2019).
[46] M. M. Otrokov, I. P. Rusinov, M. Blanco-Rey, M. Hoffmann, A. Y. Vyazovskaya, S. V. Eremeev, A. Ernst, P. M. Echenique, A. Arnau, and E. V. Chulkov, Phys. Rev. Lett. **122**, 107202 (2019).

[47] I. I. Klimovskikh, M. M. Otrokov, D. Estyunin, S. V. Eremeev, S. O. Filnov, A. Koroleva, E. Shevchenko, V. Voroshnin, A. G. Rybkin, I. P. Rusinov *et al.*, npj Quantum Mater. **5**, 54 (2020).
[48] J. Wu, F. Liu, M. Sasase, K. Ienaga, Y. Obata, R. Yukawa, K. Horiba, H. Kumigashira, S. Okuma, T. Inoshita *et al.*, Sci. Adv. **5**, eaax9989 (2019).
[49] B. Chen, F. Fei, D. Zhang, B. Zhang, W. Liu, S. Zhang, P. Wang, B. Wei, Y. Zhang, Z. Zuo *et al.*, Nat. Commun. **10**, 4469 (2019).
[50] S. Eremeev, M. Otrokov, and E. Chulkov, J. Alloys Compd. **709**, 172 (2017).
[51] See Supplemental Material at http://link.aps.org/supplemental/10.1103/PhysRevB.103.235142 for additional data and discussions.
[52] W.-H. Xie, B.-G. Liu, and D. G. Pettifor, Phys. Rev. B **68**, 134407 (2003).
[53] J. Bland and S. Basinski, Can. J. Phys. **39**, 1040 (1961).
[54] A. Andriamihaja, A. Ibanez, J.-C. Jumas, J. Olivier-Fourcade, and E. Philippot, Rev. Chim. Miner. **22**, 357 (1985).
[55] I. Teramoto and S. Takayanagi, J. Phys. Chem. Solids **19**, 124 (1961).
[56] J. Li, Y. Li, S. Du, Z. Wang, B.-L. Gu, S.-C. Zhang, K. He, W. Duan, and Y. Xu, Sci. Adv. **5**, eaaw5685 (2019).
[57] J. R. Viana and J. R. de Sousa, Phys. Rev. B **75**, 052403 (2007).
[58] N. D. Mermin and H. Wagner, Phys. Rev. Lett. **17**, 1133 (1966).
[59] J. Henk, M. Flieger, I. V. Maznichenko, I. Mertig, A. Ernst, S. V. Eremeev, and E. V. Chulkov, Phys. Rev. Lett. **109**, 076801 (2012).
[60] Y.-J. Hao, P. Liu, Y. Feng, X.-M. Ma, E. F. Schwier, M. Arita, S. Kumar, C. Hu, R. Lu, M. Zeng, Y. Wang *et al.*, Phys. Rev. X **9**, 041038 (2019).
[61] L.-X. Wang, Y. Yan, L. Zhang, Z.-M. Liao, H.-C. Wu, and D.-P. Yu, Nanoscale **7**, 16687 (2015).
[62] M. P. L. Sancho, J. M. L. Sancho, J. M. L. Sancho, and J. Rubio, J. Phys. F **15**, 851 (1985).
[63] J. Henk and W. Schattke, Comput. Phys. Commun. **77**, 69 (1993).
[64] K. Efetov and A. Larkin, Sov. Phys. JETP **41**, 76 (1975).
[65] P. E. Blöchl, Phys. Rev. B **50**, 17953 (1994).
[66] G. Kresse and J. Hafner, Phys. Rev. B **47**, 558 (1993).
[67] G. Kresse and J. Furthmüller, Phys. Rev. B **54**, 11169 (1996).
[68] G. Kresse *et al.*, Comput. Mater. Sci. **6**, 15 (1996).
[69] J. P. Perdew, K. Burke, and M. Ernzerhof, Phys. Rev. Lett. **77**, 3865 (1996).
[70] D. Koelling and B. Harmon, J. Phys. C **10**, 3107 (1977).
[71] S. Grimme, J. Antony, S. Ehrlich, and H. Krieg, J. Chem. Phys. **132**, 154104 (2010).
[72] V. I. Anisimov, J. Zaanen, and O. K. Andersen, Phys. Rev. B **44**, 943 (1991).
[73] S. L. Dudarev, G. A. Botton, S. Y. Savrasov, C. J. Humphreys, and A. P. Sutton, Phys. Rev. B **57**, 1505 (1998).
[74] M. Cococcioni and S. de Gironcoli, Phys. Rev. B **71**, 035105 (2005).
[75] A. A. Soluyanov and D. Vanderbilt, Phys. Rev. B **83**, 235401 (2011).
[76] D. Gresch, G. Autes, O. V. Yazyev, M. Troyer, D. Vanderbilt, B. A. Bernevig, and A. A. Soluyanov, Phys. Rev. B **95**, 075146 (2017).
[77] N. Marzari and D. Vanderbilt, Phys. Rev. B **56**, 12847 (1997).
[78] A. A. Mostofi, J. R. Yates, Y.-S. Lee, I. Souza, D. Vanderbilt, and N. Marzari, Comput. Phys. Commun. **178**, 685 (2008).
[79] A. Togo and I. Tanaka, Scr. Mater. **108**, 1 (2015).
[80] A. I. Liechtenstein, M. Katsnelson, V. Antropov, and V. Gubanov, J. Magn. Magn. Mater. **67**, 65 (1987).
[81] M. Hoffmann, A. Ernst, W. Hergert, V. N. Antonov, W. A. Adeagbo, R. M. Geilhufe, and H. Ben Hamed, Phys. Status Solidi B **257**, 1900671 (2020).
[82] L. Vitos, J. Kollár, and H. L. Skriver, Phys. Rev. B **49**, 16694 (1994).